Catalytic reactive flash volatilisation of microalgae to produce hydrogen or methane-rich syngas

Pratik Gholkar[a,b,c], Yogendra Shastri[b], Akshat Tanksale[c,*]

[a] IITB-Monash Research Academy, Mumbai, 400076, India
[b] Department of Chemical Engineering, Indian Institute of Technology Bombay, Mumbai, 400076, India
[c] Department of Chemical Engineering, Monash University, Clayton, Victoria, 3800, Australia

ABSTRACT

Catalytic reactive flash volatilization (RFV) is a single-step char- and tar-free alternative to the gasification process at low temperatures (600–650 °C). In this work catalytic RFV of microalgae *Scenedesmus* sp. was performed using steam as a gasifying agent. Effect of temperature and steam content on the gasification efficiency and syngas composition was studied in presence of Ni-Rh/γ-Al$_2$O$_3$ catalyst which showed that at 650 °C and carbon-to-steam ratio of 0.12, H$_2$ rich (65% (v/v)) syngas was generated, whereas, in presence of Ni-Cu-Pd/γ-Al$_2$O$_3$ catalyst at 600 °C and carbon-to-steam ratio of 0.12, CH$_4$ rich (16% (v/v)) syngas was generated. Gasification efficiency of 83% and 93%, respectively, was achieved without tar formation. Furthermore, the molar ratio of H$_2$-to-CO in case of H$_2$-rich syngas was 10.9. The alkali and alkaline earth metals present in the microalgae act as a catalyst in the reaction which lead to stable catalytic performance.

1. Introduction

One of the grand challenges of this century is to transit from fossil fuels to clean energy resources. Renewable hydrogen is a leading alternative since it is regarded as the clean source of energy. It can be produced from biomass (cellulosic, lignocellulosic and microalgal) and water. However, photovoltaic water splitting is limited by low efficiency of hydrogen production (less than 5%) [1]. Likewise, first generation biomass feedstocks are limited by food vs fuel debate and lignocellulosic biomass is limited by photosynthetic efficiency and growth potential [2]. Microalgae is one of the leading alternative feedstocks because, compared to lignocellulose, it provides a) higher CO$_2$ fixation efficiency, b) higher growth rate, c) higher photosynthetic efficiency, d) higher energy density (J/m^3), and e) ability to grow in brackish water [3–6]. However, most of the research on the utilisation of microalgae have focused on the conversion of lipids into biodiesel. The utilization of entire cell has received little attention.

Among the current conversion processes, hydrothermal liquefaction (HTL) is limited by harsh operating conditions such as high temperature (400 °C–600 °C) and high pressure (up to 280 bar) [7]. A lower efficiency of lipid extraction is the main hurdle for transesterification route [8,9]. Two step conversion of microalgae i.e. pyrolysis followed by steam reforming of oil and gasification of char is reported in the literature. However, only around 60% carbon was converted to oil.

Moreover, the process is cost intensive due to additional unit operations involved [10,11]. Kirkels and Verbong [12] have noted that biomass gasification technology to produce syngas is a promising solution for the generation of energy. Moreover, gasification has an edge over other biochemical and thermochemical conversion processes such as, HTL because it generates a product without any ringed or double bond structures. However, tar cleaning remains a challenge in the commercialisation of the gasification technology [13].

Dry microalgae gasification reports are limited in the published literature. Raheem, et al. [14] performed batch experiments on microalgae gasification and observed that a holding time of 20 min. resulted in gas, char and tar yields of 75.8%, 11.6% and 12.6%, respectively. Liu, et al. [15] showed chemical looping gasification of microalgae can be performed in the presence of the Fe$_2$O$_3$/CaO catalyst. However, the average conversion efficiency of the process was only 77%. Duman, Uddin and Yanik [16] reported only 70% tar conversion into gas in a microreactor gasification of microalgae in the presence of the Fe$_2$O$_3$/CeO$_2$ catalyst.

Salge, et al. [17] reported reactive flash volatilization of non-volatile feedstock in the presence of the Rh-Ce/α-Al$_2$O$_3$ catalyst at 800 °C resulting in tar and char-free syngas. RFV operates at higher carbon mass- and space-velocities compared to gasification and steam reforming. This implies that, RFV reactor needs smaller volumes and less quantity of catalyst compared to gasification. The advantages of RFV

---

over gasification are discussed in detail in our earlier work [18]. It was also possible to tune the ratio of H_2-to-CO in the syngas by changing the feed ratio [19,20]. However, only model components such as soy oil and cellulose were reported in their study. Our earlier work reported RFV of lignocellulosic biomass in the presence of the $Ni/\gamma Al_2O_3$ and Ni-$M/\gamma Al_2O_3$ (M = Rh, Re, Ru and Pt) catalyst. In the range of 700 °C–800 °C, at carbon-to-steam ratio (CSR) of 1.0 and carbon-to-oxygen ratio of 0.5, carbon deposition was observed on the surface of Ni catalyst resulting in the deactivation of the catalyst. Moreover, similar observations are reported in the literature for Ni catalyst [21–23]. Whereas, at 800 °C, in presence of Ni-Rh catalyst, with a CSR of 2.35 a carbon conversion efficiency of 99% was observed [24]. Moreover, Cu-Pd is known for hydrogenation of CO and CO_2 [25–27]. Hence, Ni-Rh and Ni-Cu-Pd was selected as the catalyst for hydrogen and methane production, respectively.

To date very few studies have shown single step, tar free conversion of microalgae into syngas. The effect of nitrogenous compounds found in microalgae on the gasification efficiency is unknown. Moreover, the role of alkali and alkaline earth metals (AAEM) in the reaction mechanism is not well understood. The minerals found in microalgae were very different to lignocellulose and many compounds have low melting points and are highly reactive.

This manuscript reports catalytic steam gasification of microalgae–*Scenedesmus* sp. at high space velocity using Ni-Rh/γAl_2O_3 and Ni-Cu-Pd/γAl_2O_3 catalyst. By varying the temperature and catalyst, the gas composition was found to change from H_2- to CH_4-rich syngas. A slag bed formation resulted in catalytic effect from the AAEM was established using XPS and FEGSEM analyis.

2. Materials and methods

2.1. Biomass feedstock characterisation

Scenedesmus sp.– henceforth referred as microalgae, was obtained from South Australia Research and Development Institute (SARDI). *Scenedesmus* sp. was chosen due to its higher tolerance for CO_2 which is necessary to sequester carbon from power plants. Microalgae was characterised using European standards (EN); EN14774, EN14775 and EN15148:2009 were used to analyse moisture, proximate and ultimate content of the microalgae, respectively. Table 1 shows the ultimate analysis of the microalgae.

Table 1
Ultimate analysis of microalgae.

Ultimate analysis	(% db)
C	40.3
H	7.0
N	8.1
S	1.22
Ash	10.9
O*	32.5
Ash	(%)
MgO	15.6
Al_2O_3	1.83
SiO_2	5.84
P_2O_5	51.9
SO_3	0.68
Cl	0.062
K_2O	12.6
CaO	8.6
TiO_2	0.16
MnO	0.11
Fe_2O_3	2.57
CoO	0.09
NiO	0.01
CuO	0.03
ZnO	0.04

* Calculated by difference.

2.2. Catalyst preparation

The catalysts consisting of Nickel-Rhodium (Ni-Rh/γ-Al_2O_3) and Nickel- Copper-Palladium (Ni-Cu-Pd/γ-Al_2O_3), were prepared using the wet impregnation method. Alumina (Al_2O_3) was used as a support and Rhodium chloride ($RhCl_3$), Cupric nitratetrihydrate ($CuN_2O_6.3H_2O$), Nickel nitrate hexahydrate ($Ni(NO_3)_2 \cdot 6H_2O$), all obtained from Sigma Aldrich were used as source for nickel, rhodium and copper, respectively. First, nickel nitrate hexahydrate was dissolved in deionized water, and then alumina and the precursors were added into the solution. Final concentration of nickel and rhodium in the bimetallic catalyst was 10% (w/w) and 1% (w/w), respectively. Whereas, the trimetallic catalyst was comprising of 20% (w/w) nickel, 1% (w/w) copper and 1% (w/w) palladium. The mixture was stirred at 65 °C for five hours. The suspension was dried at 100 °C, followed by, calcination at 600 °C for six hours. The resultant catalysts were reduced in-situ before analysing their catalytic activity. The catalysts were characterised for its surface area, pore size, reduction profile, and metal active sites using methods described in our earlier work [28].

2.3. Reactor setup and experimental conditions

To evaluate the catalytic activity of the catalysts, reactive flash volatilization (RFV) microalgae was performed in a bench scale fixed bed downdraft reactor explained in our earlier work [28]. In brief, it consisted of a 700 mm long quartz tube reactor with 25 mm OD fitted with a quartz frits at 350 mm. A K-Tron twin screw powder feeder (K-MVKT20), an Alltech HPLC pump (model 426), Teledyne Hasting mass flow controllers for nitrogen, a Labec vertical split tube furnace, a Brooks Instrument DLI Series evaporator and a custom-built gas-liquid separator. To perform RFV, reactor was loaded with 1 g of catalyst and assembled in the furnace. Then, the catalyst was reduced with 5% H_2/N_2 gas mixture at 400 °C for four hours. This reduction temperature was chosen sine it is higher than the onset reduction temperature found in the TPR results (section 3.1.2). Microalgae needs minimum 450 °C for devolatilization [29]. Moreover, steam and temperature exhibit a synergistic effect on the catalytic activity. Hence, range of temperature was chosen between 550 °C–650 °C and range of CSR was chosen between 0.12 to 0.8. The temperature was achieved with the ramping of 10 °C/min, whereas, CSR was controlled using the flow rate of water. The gas space velocity was adjusted using the flow rate of nitrogen. 7 g/h of microalgal biomass having 5% moisture was fed to the reactor using twin-screw feeder, to achieve the desired carbon space– and mass–velocity. Product gas was sampled periodically after gas-liquid separator and injected into GC for analysis. Shimadzu gas chromatograph GC-2014; equipped with a molecular sieve 5 A column, Thermal Conductivity Detector (TCD) and a Flame Ionisation Detector (FID) was used for gas analysis. Bubble-O-Meter was used to measure the flow rate of product gas. Carbon content of condensate and slag produced after RFV was analysed using LECO TruMac CHNS analyser. The mass of condensate and slag was measured, and the carbon content in that was then measured using the CHNS analyser. The effluent gas flow rate was measured using a bubble flow meter and the composition of carbon containing compounds was measured using a GC. This provided the basis for carbon balance. Apparent mass of gas was calculated assuming ideal gas law.

Depending on the carbon balance, gasification efficiency and yield were calculated using the following formulae

$$\text{Gasification efficiency} = \frac{\text{Moles of carbon in a gas phase}}{\text{Total moles of carbon in the feed}} \times 100 \quad (1)$$

$$\text{Gas yield} = \frac{\text{mass in gas phase}}{\text{mass of microalgae}} \times 100\% \quad (2)$$

$$\text{Char yield} = \frac{\text{mass of char}}{\text{mass of microalgae}} \times 100\% \quad (3)$$

Table 2
Elements present in the slag after reaction.

Characterization	Catalyst		
	Alumina	Ni-Rh	Ni-Cu-Pd
Surface Area (m^2/g)	1.02×10^2	8.7×10^1	8.2×10^1
Pore Volume (cm^3/g)	1.8×10^{-1}	1.7×10^{-1}	1.5×10^{-1}
XRF Characterization		Ni: 11.9% ± 0.8%	Ni: 21.5% ± 0.8%
		Rh[*]:0.92%	Cu: 1.33% ± 0.2%
			Rh[*]: 1.2%
Ni Dispersion (%)		1.03	0.01
Turnover Frequency (min^{-1})		3.31×10^2	3.69×10^3

* Calculated by difference.

$$\text{Tar yield} = \frac{\text{mass of tar}}{\text{mass of microalgae}} \times 100\% \quad (4)$$

3. Results and discussion

3.1. Catalyst characterisation

3.1.1. Nitrogen physisorption and XRF analysis

Table 2 shows the results of nitrogen physisorption, CO chemisorption and XRF analysis. It was observed, that the surface area of alumina was reduced while pore volume remained the same. XRF analysis was used to confirm the metal loading. The values reported in the Table 2 match with the theoretical calculated metal loading. CO chemisorption was conducted using pulse titration method (detailed method in ESI) which showed that Ni-Rh had a CO coverage of 22.3 μmol/g-catalyst whereas Ni-Cu-Pd catalyst had a CO coverage of only 0.3 μmol/g-catalyst. The pulse titration method underestimates the CO coverage on Pd catalysts [30]. Moreover, it is also possible that the formation of Ni-Cu alloy resulted in the modification of Ni active sites [31,32]. This is in coherence with the observation reported in TPR and XRD analysis.

3.1.2. Temperature programmed reduction (TPR)

Fig. 1 shows the TPR profiles of Ni-Cu-Pd (curve a) and Ni-Rh (curve b) catalysts. The onset of reduction for Ni-Cu-Pd and Ni-Rh catalyst was observed at 300 °C and 362 °C, respectively. It has been extensively reported in the literature, that the reducibility of Ni catalysts is promoter dependent, and it is governed by the hydrogen spill over effect
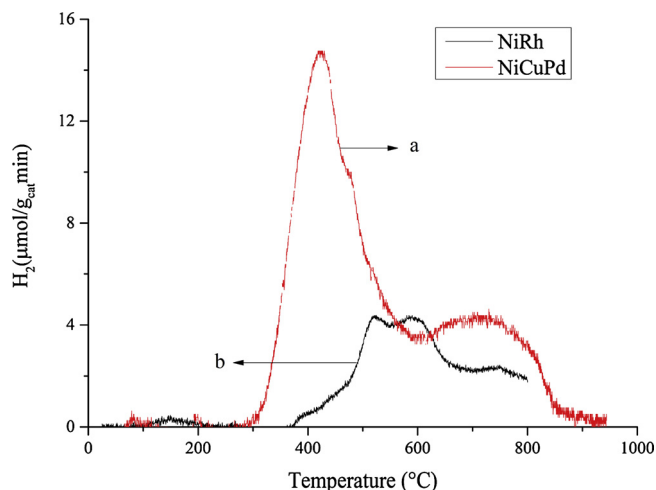

Fig. 1. TPR profile of the catalyst. a) Ni-Cu-Pd and b) Ni-Rh.

attributed by the individual promoter [33]. Curve a shows a major peak at 400 °C, a broad peak between 600 °C–800 °C and a shoulder peak around 480 °C. Whereas, curve b exhibits four peaks at 400 °C, 520 °C, 600 °C and 750 °C, respectively. Monometallic Ni on alumina support reduces at temperatures in excess of 700 °C [34]. A peak at 750 °C in curve a and a broad peak between 600 °C–800 °C in curve b is attributed to the strong interaction of Ni with the support forming Nickel Aluminate. It is well known in the literature that the interaction of Ni with alumina is strongly depended on the Ni loading. At < 12% loading, Ni interacts with the tetrahedrally coordinated sites present on alumina. In contrast, above 12% it forms NiO as a bulk phase due to alumina surface saturation [35]. A major peak at 400 °C in curve a is attributed to the bulk NiO and a shoulder peak at 480 °C is likely to be the Ni-Cu alloy reduction. Moreover, two TPR peaks at 520 °C and 600 °C in curve b can be attributed to the Nickel-alumina interaction at tetrahedrally coordinated sites. Furthermore, the phases observed during reductions are in coherence with the observations of XRD analysis as shown in the Figure S1 and Table S1.

3.1.3. Carbon monoxide temperature programmed desorption (CO-TPD)

CO desorption at elevated temperature is a complex process. The entire mechanism of CO desorption is not always fully understood. The desorption is mainly dependent on a) activation energy and b) surface area coverage by CO [36]. Figure S2 shows the TPD profile for Ni-Cu-Pd catalyst and the TPD profile for Ni-Rh catalyst can be found in our earlier work [28]. Curve (a) in Figure S2 indicates desorption of CO and curve (b) in Figure S2 denotes the evolution of CO_2. CO_2 is formed on the surface of the alumina catalyst by reacting with the hydroxyl groups on the surface of alumina [36]. Weak multilayer adsorption of CO on the catalyst surface resulted into the early low temperature peak at 50 °C. However, strong single layer CO adsorption resulted into the dominant peak at approximately 160 °C.

3.2. Effect of steam and temperature on the gas composition

Fig. 2 shows that at 600 °C and in presence of Ni-Rh catalyst the composition of H_2 and CO decreased, and the composition of CO_2 increased with decreasing the carbon-to-steam ratio (CSR) which is likely due to the competing reaction equilibria of water gas shift and CO methanation reaction. Although, at CSR of 0.8 the composition of CH_4 and H_2 was high (16% and 45%) the reactor clogged after 3 h of operation because of char and tar accumulation. The steam content was not enough for char gasification and tar reformation. Similarly, as shown in Fig. 3 at CSR of 0.12 and temperature 550 °C, although the composition of H_2 and CH_4 was high (55% and 15%, respectively) the reactor clogged after 2.5 h of operation. The operating temperature was not enough for char gasification and tar reformation. Although, the gasification efficiency was improved when CSR was changed from 0.8 to 0.2 (Figure S3), the operational time was limited to 4 h due to tar accumulation. As shown in Fig. 3, at 650 °C in presence of Ni-Rh catalyst and CSR of 0.12, 65% (v/v) H_2 was produced with the gasification efficiency of more than 95% (Figure S4) The composition of H_2 is 60% more than the hydrogen composition reported by Xie, Duan, Jiao and Xu [37] during hydrothermal gasification. The reactor was operational for 9 h with an average rate of reaction of 7.38 mmol ·min^{-1} ·g-catalyst^{-1}, giving a turn over frequency (TOF) of 330.94 min^{-1} based on the CO-coverage measured using pulse titration method. The yield of hydrogen was calculated to be 118.46 g H_2/ kg microalgae. Moreover, the overall yield of gas, char and tar on condensate and ash free basis was calculated to be 95%, 3% and 1%, respectively. The yield of hydrogen obtained is 97% higher compared to catalytic HTL process reported in the literature [38]. The monometallic Ni catalyst was not stable in the reaction conditions, leading to quick deactivation before stable operating conditions could be achieved, and hence it was not possible for us to estimate the TOF of the reaction over Ni/alumina catalyst. The effect of the promoter is to keep the Ni surface clean by
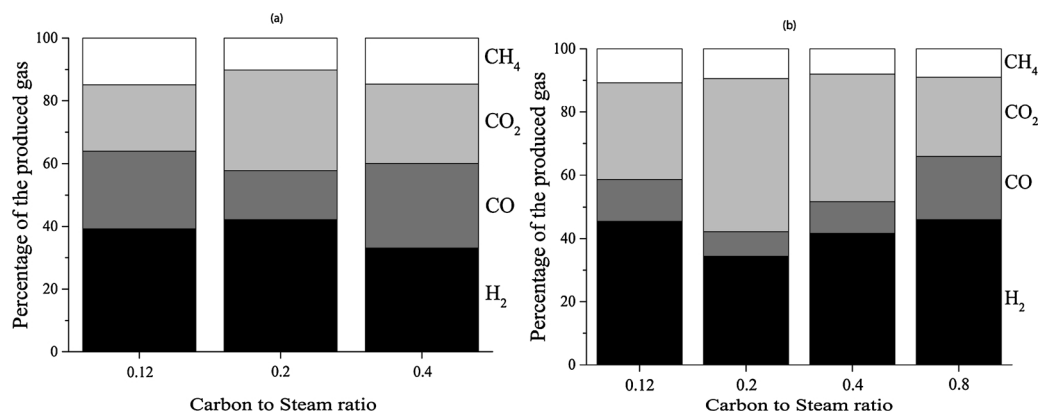
Fig. 2. Effect of steam content on the distribution of the compounds in the syngas. Operating conditions: Temp: 600 °C, feeding rate: 7 g/h, (a) Ni-Cu-Pd/Al₂O₃ and (b) Ni-Rh/Al₂O₃.

promoting tar reforming and preventing coke deposition. The composition of H_2 was enhanced most likely due to enhancement of water gas shift and methane steam reforming reactions [39–41].

In presence of Ni-Cu-Pd catalyst (Fig. 3), composition of CH_4 was observed to be 16% at 550 °C and 600 °C. However, at 550 °C the reactor clogged after 3.5 h, whereas, at 600 °C the reactor was operational for 13 h with the gasification efficiency of 85% (Figure S4). Based on the CO-coverage measured using pulse titration method, the TOF of the catalyst was calculated to be 3.69×10^3 min^{-1}. The relatively high TOF calculated here may be due to the limitation of pulse titration method for measuring CO-coverage for Pd catalysts [30] and lower CO-coverage measured due to Ni-Cu alloy formation. The yield of CH_4 was calculated to be 174.24 g CH_4/ kg microalgae. Moreover, the overall yield of gases, char and tar on condensate and ash free basis was calculated to be 95%, 3.2% and 1%, respectively. Ni-Cu-Pd catalyst promoted methanation reaction via hydrogenation of CO and CO_2 resulting in low hydrogen-to-carbon monoxide ratio which is consistent with literature (Fig. 4) [42,43]. While the effect of Rh promoter was to enhance the reforming and WGS reactions, leading to high H_2 selectivity, the effect of Cu-Pd promoter was to enhance the methanation reaction. This compares favourably with the published literature. Raheem, et al. [14] reported gasification of Chlorella vulgaris with the efficiency of 75% and product gas composition consisting of 22.2% CH_4 and 24.2% H_2. Liu, et al. [15] reported gasification efficiency of 77.19% and product gas composition consisting of 9% CH_4 and 17% H_2 using chemical looping gasification of Chlorella vulgaris.

3.3. Ash transformation characteristics

Boström, et al. [44] classified the ash into two groups silica- and phosphorus-rich ash. Further it is also classified into subgroups such as high potassium or calcium containing ash based on the ratio of potassium to calcium. Woody biomass falls into the category of silica rich, high calcium containing ash [44]. Whereas, based on the composition described in the Table 1, microalgae can be classified as phosphorus rich, high potassium containing ash. Transformation of high silica containing ash is well reported in the literature. Bostrom, et al. [45] and He, et al. [46] articulated that, the silicates of the alkali and alkaline earth metals (AAEM) are formed during ash transformation depending on the operating temperature of the reactor. However, the transformation of phosphorous rich ash is not extensively reported in the literature. Skoglund [47] has explained the potential reaction mechanism involved in the ash transformation. They have noted that, formation of AAEM phosphates is a three-step process consisting of oxidation, neutralization and phosphorylation. The Ellingham diagram for the participating elements shows that the reactivity of the potassium and magnesium is much higher compared to the silica and calcium [48,49]. The details pertaining to the reactions and their sequence leading to AAEM phosphate formation can be found elsewhere [47]. It was observed from the XRD pattern shown in Figure S5, that the crystalline ash was transformed into an amorphous slag. Table S2 lists the compounds that were identified based on the XRD analysis of ash and slag. It was evident that, AAEM elements have transformed into their respective phosphates during the reaction. To confirm the transformation of AAEM elements, XPS analysis of slag was performed. XPS profiles of Phosphorus, Potassium and Magnesium are shown in Figure S6, Figure
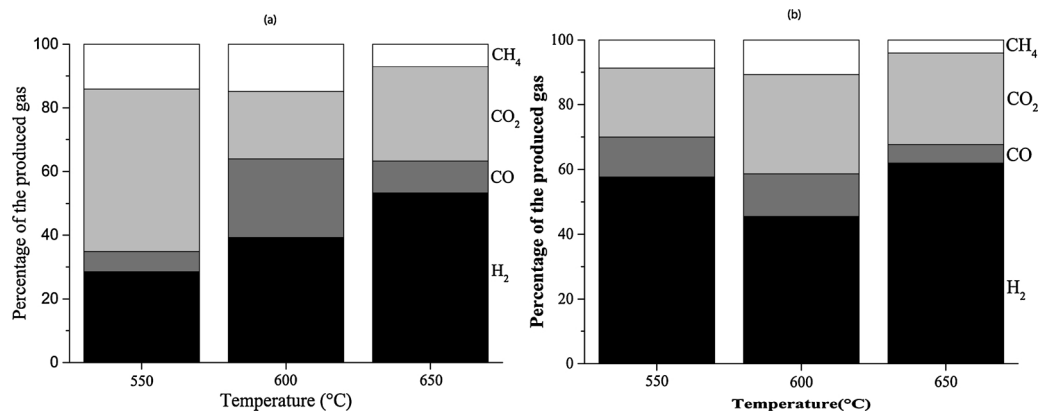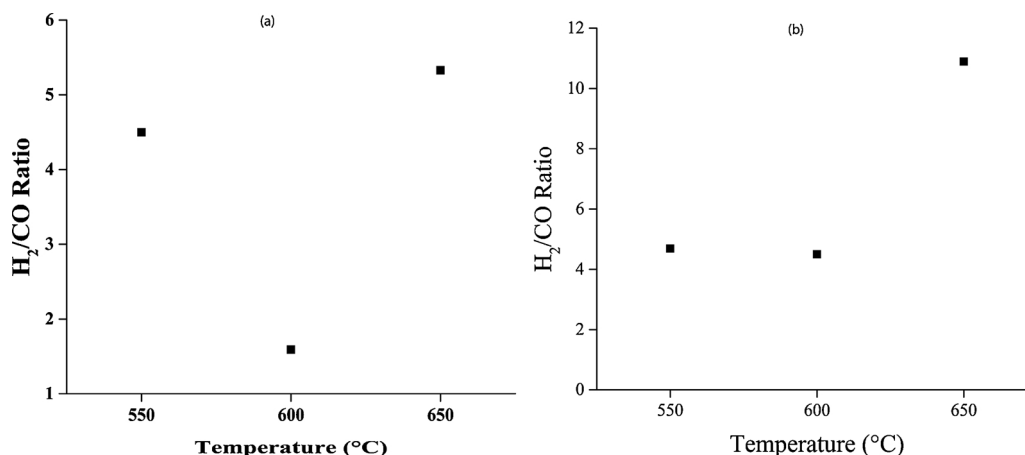

Fig. 3. Effect of temperature on the distribution of the compounds in the syngas. Operating conditions: C/S: 0.12, feeding rate: 7 g/h, (a) Ni-Cu-Pd/Al₂O₃, (b) Ni-Rh/Al₂O₃).

Fig. 4. Effect of temperature on the distribution of the ratio of hydrogen to carbon monoxide (H_2/CO). Operating conditions: C/S: 0.12, feeding rate: 7 g/h, (a) Ni-Cu-Pd/Al_2O_3, (b) Ni-Rh/Al_2O_3.
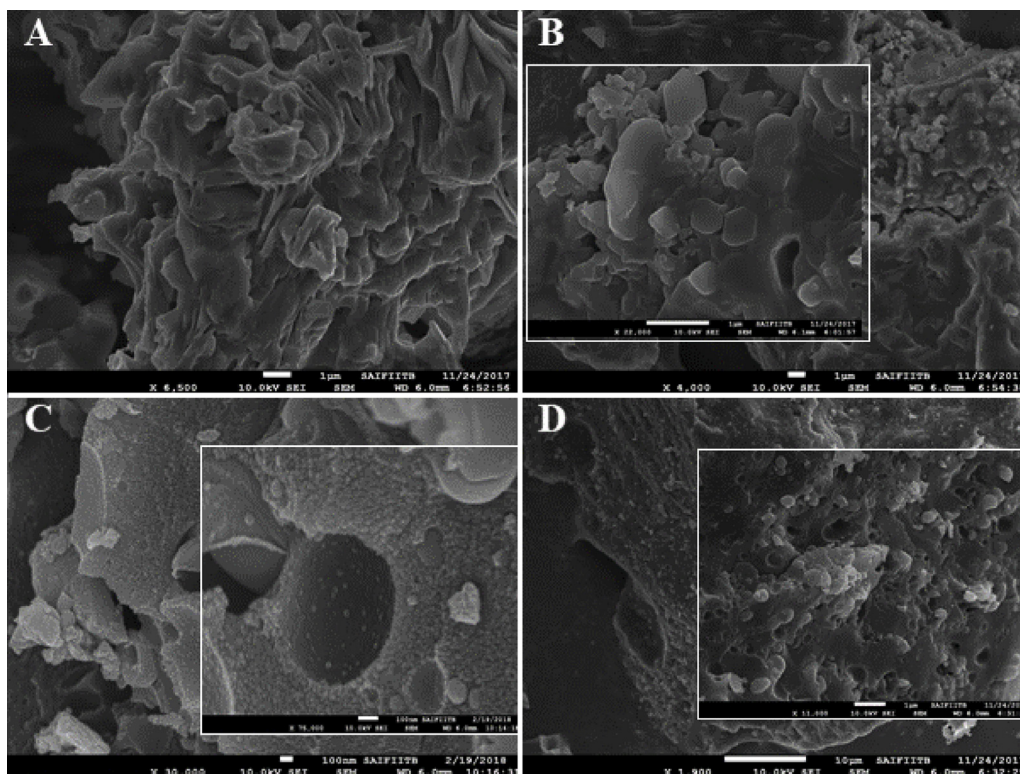
Table 3
XPS analysis of ash and slag.

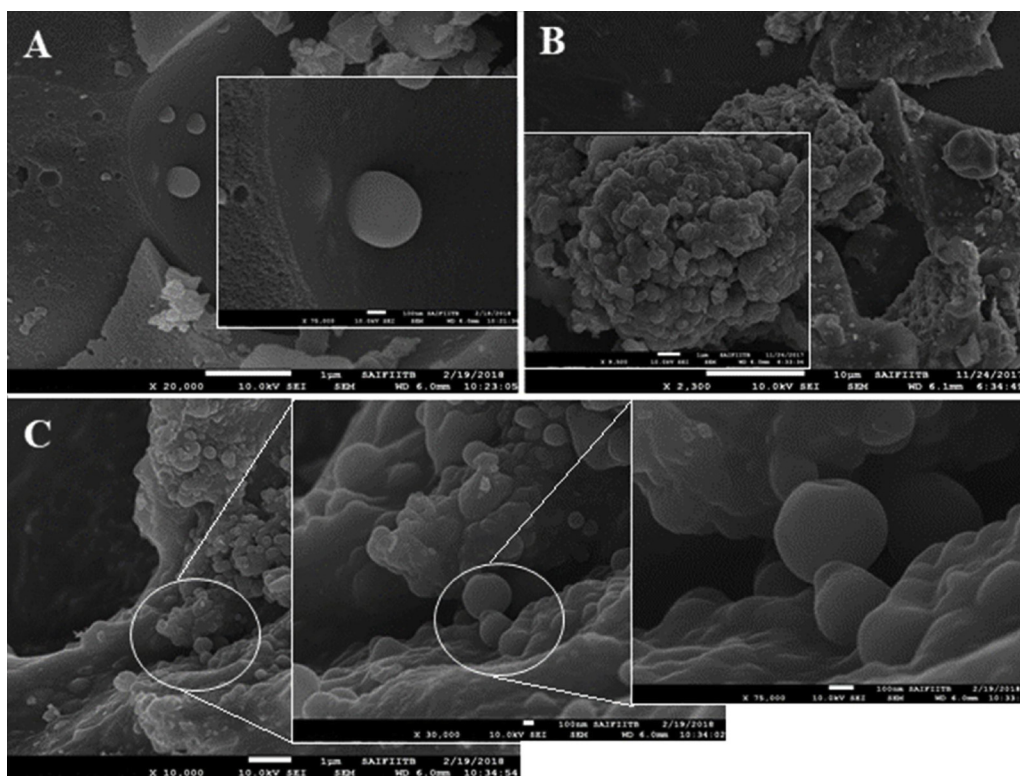| Element	Ash (eV)	Slag (eV)	Shift (eV)
P	2p1/2: 133.67	2p1/2: 133.15	2p1/2: 0.52
	2p3/2:132.81	2p3/2: 132.29	2p3/2: 0.52
K	2s: 377.42	2s: 376.86	2s: 0.56
Mg	1s: 1302.65	1s: 1303.42	1s: 0.77

S7 and Figure S8, respectively. A shift in the binding energy of the elements is observed and it is summarized in Table 3. Transformation in the chemical nature of the elements resulted into altered morphology, which was confirmed using FEG-SEM analysis. Fig. 5A and B shows non-porous surface with random arrangements of crystals and sheets. Whereas, Fig. 5C and D shows a porous structure made up of small

beads. Furthermore, as shown in Figure S9, SEM-EDX analysis has confirmed the presence of Ca, Mg, P and K in the naosphere formed during ash transformation.
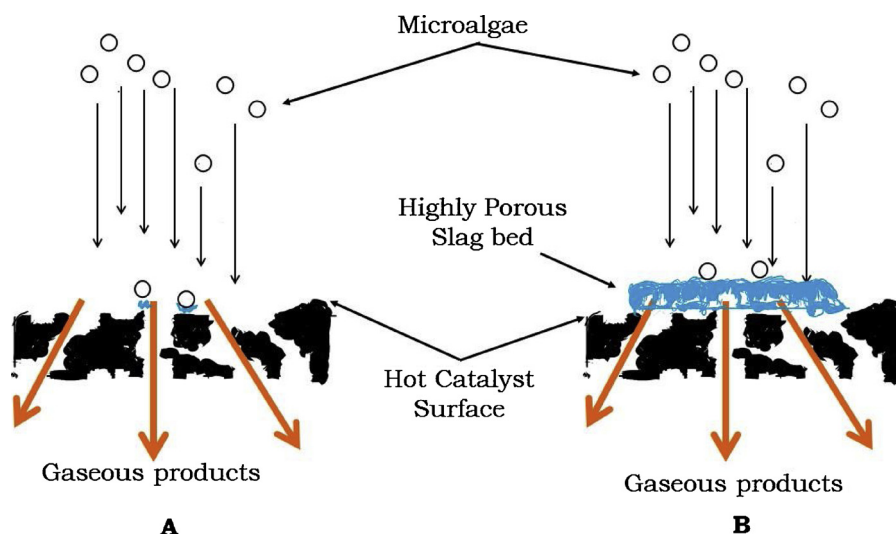
We hypothesize that, an agglomeration of potassium- and magnesium- phosphate coated nano-spheres of calcium phosphates resulted into a porous morphology as shown in Fig. 6. Moreover, the bed exhibits some catalytic properties due to its composition. Potassium is an electropositive element and it enhances the WGS reaction by dissociating CO from the adsorbed sites. This results into higher hydrogen selectivity in the gas. It also enhances the surface methanation reactions. In case of magnesium, though its role in tar reforming is briefly mentioned in the literature, the exact mechanism of magnesium catalysed gasification reactions is not extensively reported in the literature. The enhanced overall catalytic activity in a reactor could be a reason for tar free conversion of microalgae. The exact role of the ash transformation in reaction mechanism and the effect of operating parameters

Fig. 5. SEM Figures showing a morphological comparison of ash before reaction (A and B) and after reaction-slag (C and D).

Fig. 6. SEM Figure showing evolution of highly porous structure of a slag. (A) Development of nanoparticle which grows into (B) agglomeration of nanoparticles to form a bead and C) evolution of a porous structure.

Fig. 7. Proposed mechanism for reactive flash volatilization of microalgae. (A) Shows catalyst bed at the start of RFV run and (B) shows the formation of slag bed on top of the catalyst after few hours of operation.

on the catalytic activity is discussed in the following sub-section.

3.4. Reaction mechanism

The RFV progresses through a series of chemical reactions. The sequence of these reactions is not fully understood. RFV was characterised by two different reaction mechanisms in the literature depending on the physical state of a feedstock [17,19]. In case of liquid feedstock, such as soy oil, the dynamics of a simultaneously boiling and cracking of a droplet on a hot porous surface is a complex mechanism. The droplet partly behaves according to the 'Leidenfrost effect'. In conventional Leidenfrost effect a vapour layer forms around the droplet of volatile

liquid as soon as it hits a hot surface. This layer insulates the droplet from the heat for a short period of time. RFV cannot be explained completely depending on this effect or film boiling, because; rapid heat transfer to the droplet will cool down the catalyst surface. In order to explain this phenomenon, Salge, et al. [17] postulated that cold drop hits the hot catalytic surface and rebounds due to momentum transfer. A rapid heat flux causes the split and instantaneous vaporization followed by, oxidative pyrolysis; to form a layer of gases around the drop. Volatile organic compounds (VOC) and gases formed then react to maintain the temperature of the catalyst to sustain the steady state of the reactor.

In case of solid feedstock such as cellulose, Colby, et al. [19] noted

that each step towards the conversion is complex combination of multi-step and multi-phase reaction with various modes of heat transfers. The process is complex due to simultaneous transfer of mass and energy. Moreover, they postulated that the reaction starts only when the cellulose particles hits the catalyst sur face, because temperature in the reactor above catalyst is not sufficient for the pyrolysis of the particle. We observed that the postulation pertaining to the reaction mechanism explained by Colby, et al. [19] holds good in the case of ash free feedstock like cellulose. However, in case of ash rich feedstock such as microalgae, ash transformation characteristics plays a critical role in ensuring the suitability of the biomass for gasification.

Fig. 7 shows the proposed mechanism for RFV of Phosphorus rich biomass. Fig. 7A depicts the state of the catalyst surface during the initial hours of the experiment, where cold microalgae particles hit the hot catalyst surface and pyrolyse into gaseous compounds and ash. These gaseous compounds react on the surface and in the bed of the catalyst leaving behind the ash. Since, the temperature of the reaction is not high enough to melt the ash particles, they form phosphates or silicates of AAEM elements by absorbing the thermal energy [45]. This chemical shift in the ash compounds leads to the formation of highly porous structure on top of the catalyst bed as shown in Fig. 7B. The formation of porous bed on top of the catalyst was confirmed using an optical image and X-ray CT as shown in Fig. 8. Figs. 8b (A) to (F) represent an angular rotation of the sample along the Z-axis and it is clear from the figures that it is a porous, loosely held irregular arrangement of the slag particles. The bed formed due to the ash transformation conducts the heat upwards. This results into a temperature gradient across the slag bed. We hypothesized that, the moment microalgae come in the contact with a hot slag bed, it pyrolyses to form oils and gases. The gaseous compounds flow through the porous bed, and the oils are reformed into gases in the presence of steam as they trickled through the bed. The degradation of oils starts at around 420 °C, whereas, the reaction temperature in the centre of the catalyst bed is well in excess of 500 °C at all the conditions tested in this work. [50] The gases then come in contact with the catalyst leading to a further gas phase reaction, the gas phase selectivity depends upon the catalyst and the operating conditions .

3.5. Catalyst stability

TEM and STEM-EDX was used to confirm the particle size and to map the distribution of the elements on the surface of the catalyst (Figs. 9 and 10). Ni-Cu-Pd catalyst nanoparticles were in the range of 30 nm–50 nm were present in the fresh catalyst (Fig. 9a) and in case of Ni-Rh, the nanoparticles were in the range of 10 nm–30 nm (Fig. 10a). EDX of Ni and noble elements depicts the co-location of nanoparticles, possibly in the form of nano-alloy. However, synchrotron analysis of Extended X-ray Absorption Fine Structure (EXAFS) elucidation is required to confirm the alloy formation. Figure 19b shows that the particle size distribution of the used Ni-Cu-Pd catalyst is unchanged compared to the fresh catalyst, while in Fig. 10b there is evidence of slight sintering on Ni-Rh nanoparticles. As shown in Figure S10, the average rate of H_2 production was maintained at 7.38 mmol min·g-catalyst^{-1-1} with a standard deviation of 0.55 mmol $\cdot$min^{-1} $\cdot$g-catalyst^{-1}, whereas, the average rate of CH_4 production was maintained at 0.63 mmol $\cdot$min^{-1} $\cdot$g-catalyst^{-1} with a standard deviation of 0.13 mmol $\cdot$min^{-1} $\cdot$g-catalyst^{-1} after 9 h and 13 h of operation, respectively. This shows that the Ni-Rh catalyst was stable for at least 9 h and Ni-Cu-Pd catalyst was stable for at least 13 h.

4. Conclusions

The results of this work show that reaction equilibrium and gas phase selectivity can be tuned in a single reactive flash volatilization reactor with high carbon space- and mass-velocities (450 mol L^{-1} h^{-1} and 7 h^{-1}, respectively). Tar free conversion of microalgae was achieved to produce hydrogen- and methane-rich syngas using Ni-Rh and Ni-Cu-Pd catalyst, respectively. 16% CH_4 and 65% H_2 was observed in a single step, tar free conversion of microalgae with H_2/CO ratio of 10.9 in a case of hydrogen-rich syngas. The overall gasification efficiency of the process was more than 90% with both Ni-Rh and Ni-Cu-Pd catalyst, while retaining its activity for at least 9 h and 13 h, respectively. The reaction mechanism for RFV of phosphorus rich microalgae showed that the conversion of ash into phosphates resulted in enhancement of the tar conversion efficiency. The AAEM elements in the
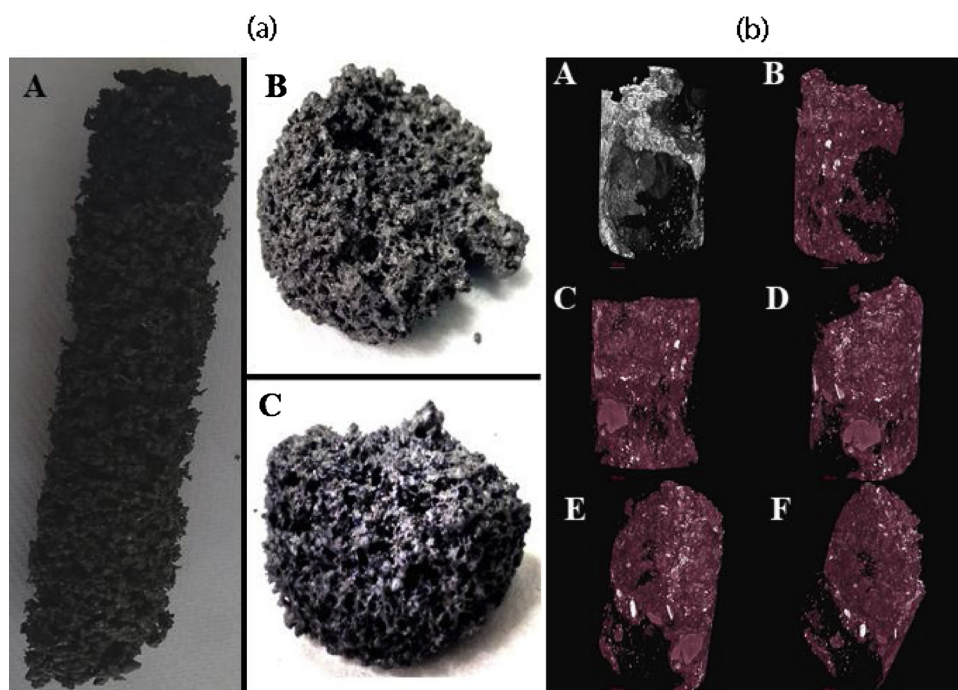

Fig. 8. Image showing a slag bed formed in the reactor during RFV of microalgae. (a) Optical images of (A) porous slag bed formed on top of the catalyst (B) top view of the slag bed C) side view of the slag bed and (b) X-ray tomography images of the slag at various rotation angles.
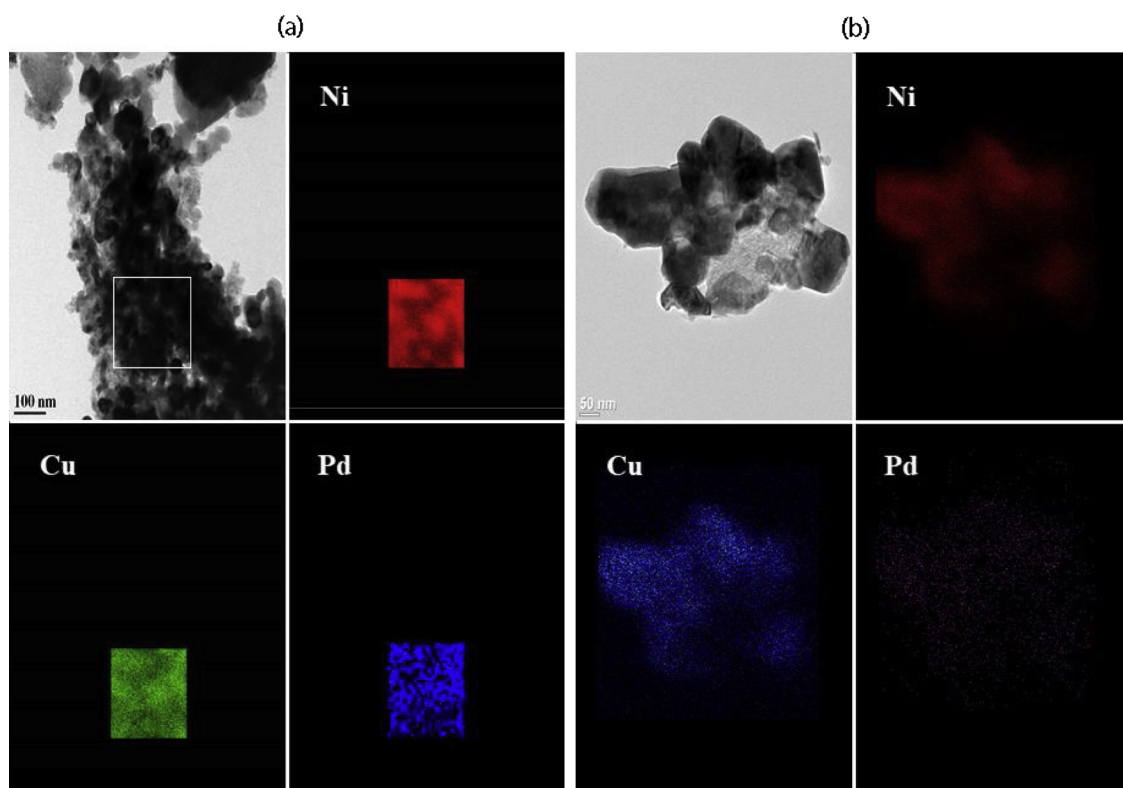
Fig. 9. STEM image of (a) fresh and (b) used Ni-Cu-Pd catalyst showing the presence of Nickel, Copper, and Palladium on the surface.
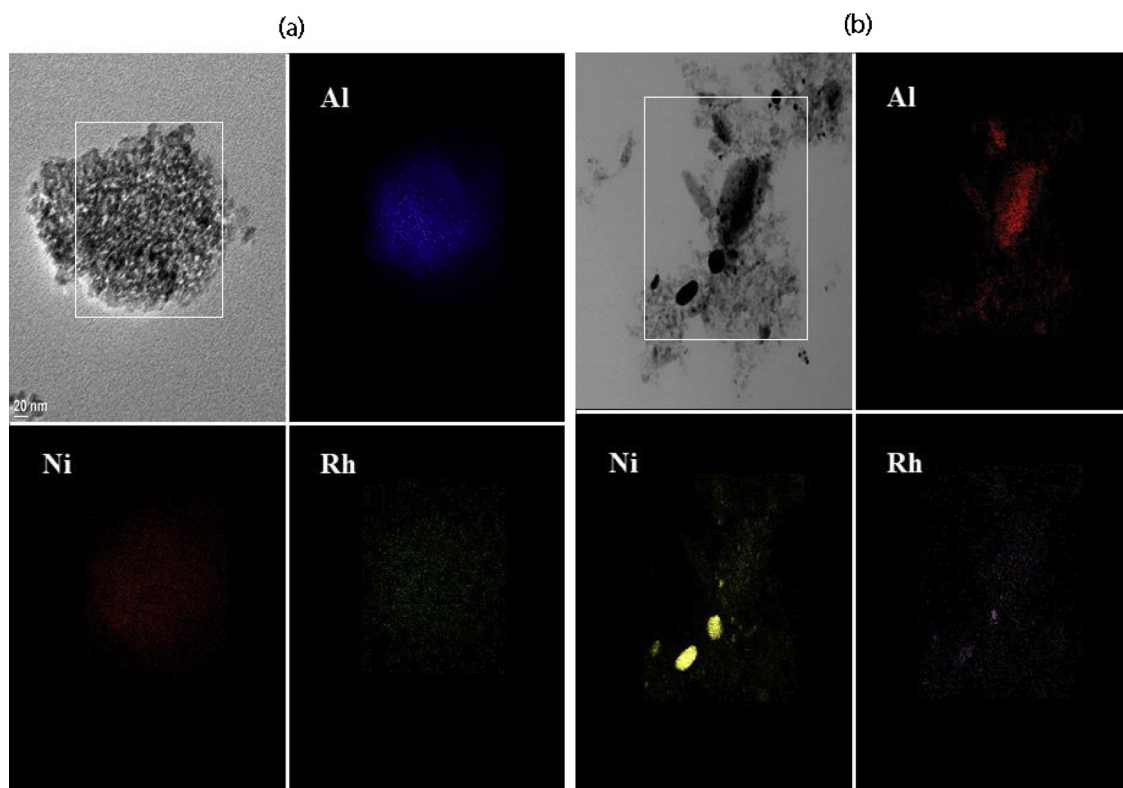

Fig. 10. STEM image of (a) fresh and (b) used Ni-Rh catalyst showing the presence of Nickel, Rhodium, and Aluminium on the surface.

ash play an important role in in-situ tar conversion by promoting steam reforming reaction.

Appendix A. Supplementary data

Supplementary material related to this article can be found, in the online version, at doi:https://doi.org/10.1016/j.apcatb.2019.03.082.

References

[1] I. Dincer, Green methods for hydrogen production, Int. J. Hydrogen Energy 37 (2012) 1954–1971.

[2] K. Wang, R.C. Brown, Catalytic pyrolysis of microalgae for production of aromatics and ammonia, Green Chem. 15 (2013) 675–681.

[3] L. Brennan, P. Owende, Biofuels from microalgae—a review of technologies for production, processing, and extractions of biofuels and co-products, Renew. Sustain. Energy Rev. 14 (2010) 557–577.

[4] B.E. Rittmann, Opportunities for renewable bioenergy using microorganisms, Biotechnol. Bioeng. 100 (2008) 203–212.

[5] J.N. Rosenberg, G.A. Oyler, L. Wilkinson, M.J. Betenbaugh, A green light for engineered algae: redirecting metabolism to fuel a biotechnology revolution, Curr. Opin. Biotechnol. 19 (2008) 430–436.

[6] Y. Chisti, Biodiesel from microalgae, Biotechnol. Adv. 25 (2007) 294–306.

[7] T.M. Brown, P. Duan, P.E. Savage, Hydrothermal liquefaction and gasification of Nannochloropsis sp, Energy Fuels 24 (2010) 3639–3646.

[8] E.M. Grima, E.H. Belarbi, F.G.A. Fernández, A.R. Medina, Y. Chisti, Recovery of microalgal biomass and metabolites: process options and economics, Biotechnol. Adv. 20 (2003) 491–515.

[9] T.M. Mata, A.A. Martins, N.S. Caetano, Microalgae for biodiesel production and other applications: a review, Renew. Sustain. Energy Rev. 14 (2010) 217–232.

[10] X. Miao, Q. Wu, C. Yang, Fast pyrolysis of microalgae to produce renewable fuels, J. Anal. Appl. Pyrolysis 71 (2004) 855–863.

[11] K. Wang, R.C. Brown, S. Homsy, L. Martinez, S.S. Sidhu, Fast pyrolysis of micro-algae remnants in a fluidized bed reactor for bio-oil and biochar production, Bioresour. Technol. 127 (2013) 494–499.

[12] A.F. Kirkels, G.P.J. Verbong, Biomass gasification: still promising? A 30-year global overview, Renew. Sustain. Energy Rev. 15 (2011) 471–481.

[13] R.M. Swanson, A. Platon, J.A. Satrio, R.C. Brown, Techno-economic analysis of biomass-to-liquids production based on gasification, Fuel 89 (2010) S11–S19.

[14] A. Raheem, V. Dupont, A.Q. Channa, X. Zhao, A.K. Vuppaladadiyam, Y.-H. Taufiq-Yap, M. Zhao, R. Harun, Parametric characterization of air gasification of Chlorella vulgaris biomass, Energy Fuels 31 (2017) 2959–2969.

[15] G. Liu, Y. Liao, Y. Wu, X. Ma, L. Chen, Characteristics of microalgae gasification through chemical looping in the presence of steam, Int. J. Hydrogen Energy 42 (2017) 22730–22742.

[16] G. Duman, M.A. Uddin, J. Yanik, Hydrogen production from algal biomass via steam gasification, Bioresour. Technol. 166 (2014) 24–30.

[17] J.R. Salge, B.J. Dreyer, P.J. Dauenhauer, L.D. Schmidt, Renewable hydrogen from nonvolatile fuels by reactive flash volatilization, Science 314 (2006) 801–804.

[18] F.L. Chan, A. Tanksale, Review of recent developments in Ni-based catalysts for biomass gasification, Renew. Sustain. Energy Rev. 38 (2014) 428–438.

[19] J.L. Colby, P.J. Dauenhauer, L.D. Schmidt, Millisecond autothermal steam reforming of cellulose for synthetic biofuels by reactive flash volatilization, Green Chem. 10 (2008) 773–783.

[20] P.J. Dauenhauer, Millisecond Autothermal Catalytic Reforming of Carbohydrates for Synthetic Fuels by Reactive Flash Volatilization, PhD Thesis University of Minnesota, 2008.

[21] L. Santamaria, G. Lopez, A. Arregi, M. Amutio, M. Artetxe, J. Bilbao, M. Olazar, Stability of different Ni supported catalysts in the in-line steam reforming of bio-mass fast pyrolysis volatiles, Appl. Catal. B: Environ. 242 (2019) 109–120.

[22] A. Ochoa, A. Arregi, M. Amutio, A.G. Gayubo, M. Olazar, J. Bilbao, P. Castaño, Coking and sintering progress of a Ni supported catalyst in the steam reforming of biomass pyrolysis volatiles, Appl. Catal. B: Environ. 233 (2018) 289–300.

[23] L. Santamaria, G. Lopez, A. Arregi, M. Amutio, M. Artetxe, J. Bilbao, M. Olazar, Influence of the support on Ni catalysts performance in the in-line steam reforming of biomass fast pyrolysis derived volatiles, Appl. Catal. B: Environ. 229 (2018) 105–113.

[24] F.L. Chan, A. Tanksale, Catalytic steam gasification of pinewood and eucalyptus sawdust using reactive flash volatilization, Appl. Catal. B: Environ. 187 (2016) 310–327.

[25] T. Fujitani, M. Saito, Y. Kanai, T. Watanabe, J. Nakamura, T. Uchijima, Development of an active Ga2O3 supported palladium catalyst for the synthesis of methanol from carbon dioxide and hydrogen, Appl. Catal. A Gen. 125 (1995) L199–L202.

[26] X. Jiang, N. Koizumi, X. Guo, C. Song, Bimetallic Pd–Cu catalysts for selective CO2 hydrogenation to methanol, Appl. Catal. B: Environ. 170 (2015) 173–185.

[27] L. Fan, K. Fujimoto, Development of an active and stable ceria-supported palladium catalyst for hydrogenation of carbon dioxide to methanol, Appl. Catal. A Gen. 106 (1993) L1–L7.

[28] F.L. Chan, A. Tanksale, Catalytic steam gasification of cellulose using reactive flash volatilization, ChemCatChem 6 (2014) 2727–2739.

[29] L. Sanchez-Silva, D. López-González, A.M. Garcia-Minguillan, J.L. Valverde, Pyrolysis, combustion and gasification characteristics of Nannochloropsis gaditana microalgae, Bioresour. Technol. 130 (2013) 321–331.

[30] G. Prelazzi, M. Cerboni, G. Leofanti, Comparison of H-2 adsorption, O-2 adsorption, H-2 titration, and O-2 titration on supported palladium catalysts, J. Catal. 181 (1999) 73–79.

[31] J. Zieliński, Studies of Ni—Cu catalysts with parallel chemisorption of O2 and de-composition of N2O, J. Mol. Catal. 49 (1988) 71–83.

[32] V. Nichele, M. Signoretto, F. Pinna, E. Ghedini, M. Compagnoni, I. Rossetti, G. Cruciani, A. Di Michele, Bimetallic Ni–Cu catalysts for the low-temperature ethanol steam reforming: importance of metal–support interactions, Catal. Letters 145 (2015) 549–558.

[33] L.P.R. Profeti, E.A. Ticianelli, E.M. Assaf, Production of hydrogen via steam re-forming of biofuels on Ni/CeO2–Al2O3 catalysts promoted by noble metals, Int. J. Hydrogen Energy 34 (2009) 5049–5060.

[34] A. Tanksale, J.N. Beltramini, J.A. Dumesic, G.Q. Lu, Effect of Pt and Pd promoter on Ni supported catalysts—a TPR/TPO/TPD and microcalorimetry study, J. Catal. 258 (2008) 366–377.

[35] C. Li, Y.-W. Chen, Temperature-programmed-reduction studies of nickel oxide/alumina catalysts: effects of the preparation method, Thermochim. Acta 256 (1995) 457–465.

[36] D.O. Hayward, B.M.W. Trapnell, Chemisorption Butterworths, London (1964).

[37] L.-F. Xie, P.-G. Duan, J.-L. Jiao, Y.-P. Xu, Hydrothermal gasification of microalgae over nickel catalysts for production of hydrogen-rich fuel gas: effect of zeolite supports, Int. J. Hydrogen Energy (2018).

[38] R. Cherad, J. Onwudili, P. Biller, P. Williams, A. Ross, Hydrogen production from the catalytic supercritical water gasification of process water generated from hy-drothermal liquefaction of microalgae, Fuel 166 (2016) 24–28.

[39] J. Guo, H. Lou, H. Zhao, D. Chai, X. Zheng, Dry reforming of methane over nickel catalysts supported on magnesium aluminate spinels, Appl. Catal. A Gen. 273 (2004) 75–82.

[40] C. Wheeler, A. Jhalani, E.J. Klein, S. Tummala, L.D. Schmidt, The water–gas-shift reaction at short contact times, J. Catal. 223 (2004) 191–199.

[41] H.Y. Wang, E. Ruckenstein, Carbon dioxide reforming of methane to synthesis gas over supported rhodium catalysts: the effect of support, Appl. Catal. A Gen. 204 (2000) 143–152.

[42] Y. Liu, D. Liu, Study of bimetallic Cu–Ni/γ-Al2O3 catalysts for carbon dioxide hy-drogenation, Int. J. Hydrogen Energy 24 (1999) 351–354.

[43] Y. Kitayama, Y. Watanabe, K. Muramatsu, T. Kodama, Catalytic reduction of carbon dioxide on Ni □ Cu alloys, Energy 22 (1997) 177–182.

[44] D. Boström, M. Boström, N. Skoglund, C. Boman, R. Backman, M. Öhman, A. Grimm, Ash transformation chemistry during energy conversion of biomass, International Conference on Impact of Fuel Quality on Power Production and the Environment, (2010).

[45] D. Bostrom, G. Eriksson, C. Boman, M. Ohman, Ash transformations in fluidized-bed combustion of rapeseed meal, Energy Fuels 23 (2009) 2700–2706.

[46] Z. He, D.J. Lane, W.L. Saw, P.J. van Eyk, G.J. Nathan, P.J. Ashman, Ash–Bed ma-terial interaction during the combustion and steam gasification of australian agri-cultural residues, Energy Fuels 32 (2018) 4278–4290.

[47] N. Skoglund, Ash Chemistry and Fuel Design Focusing on Combustion of Phosphorus-rich Biomass, (2014).

[48] A. Grimm, N. Skoglund, D. Boström, C. Boman, M. Öhman, Influence of phosphorus on alkali distribution during combustion of logging residues and wheat straw in a bench-scale fluidized bed, Energy Fuels 26 (2012) 3012–3023.

[49] A. Grimm, N. Skoglund, D. Boström, M. Ohman, Bed agglomeration characteristics in fluidized quartz bed combustion of phosphorus-rich biomass fuels, Energy Fuels 25 (2011) 937–947.

[50] A. Marcilla, A. Gómez-Siurana, C. Gomis, E. Chápuli, M.C. Catalá, F.J. Valdés, Characterization of microalgal species through TGA/FTIR analysis: application to nannochloropsis sp, Thermochim. Acta 484 (2009) 41–47.